

VGLD: Visually-Guided Linguistic Disambiguation for Monocular Depth Scale Recovery

Bojin Wu¹, Jing Chen¹*

School of Physics and Optoelectronic Engineering,
Guangdong University of Technology
Guangzhou, 510000, China
realpakinwu@gmail.com, jchen125@gdut.edu.cn

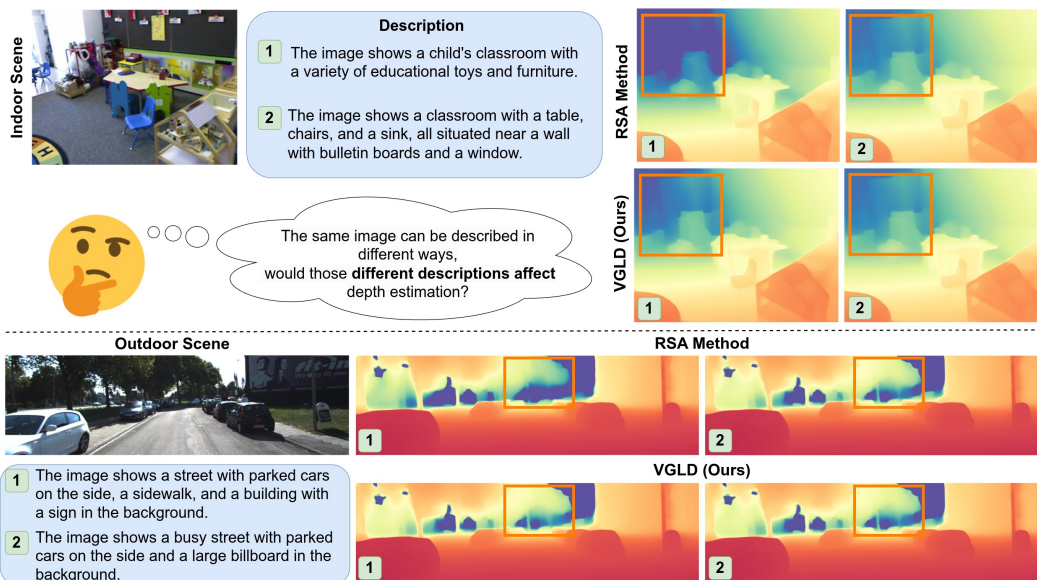


Figure 1: As observed in the figure above, a single image can have multiple different descriptions, and these varying descriptions can significantly affect depth estimation. In particular, the orange bounding boxes in the depth estimation maps highlight this issue, especially for the RSA method, where two semantically similar text descriptions result in substantial differences in depth estimation. In contrast, VGLD(ours) demonstrates relatively stable performance across different descriptions.

Abstract

We propose a robust method for monocular depth scale recovery. Monocular depth estimation can be divided into two main directions: (1) relative depth estimation, which provides normalized or inverse depth without scale information, and (2) metric depth estimation, which involves recovering depth with absolute scale. To obtain absolute scale information for practical downstream tasks, utilizing textual information to recover the scale of a relative depth map is a highly promising approach. However, since a single image can have multiple descriptions from different perspectives or with varying styles, it has been shown that different textual descriptions can significantly affect the scale recovery process. To address this issue, our method, VGLD, stabilizes the influence of textual information by incor-

*Corresponding authors.

porating high-level semantic information from the corresponding image alongside the textual description. This approach resolves textual ambiguities and robustly outputs a set of linear transformation parameters (scalars) that can be globally applied to the relative depth map, ultimately generating depth predictions with metric-scale accuracy. We validate our method across several popular relative depth models (MiDas, DepthAnything), using both indoor scenes (NYUv2) and outdoor scenes (KITTI). Our results demonstrate that VGLD functions as a universal alignment module when trained on multiple datasets, achieving strong performance even in zero-shot scenarios. Code is available at: <https://github.com/pakinwu/VGLD>

1 Introduction

Monocular depth estimation is a fundamental and long-standing task in computer vision, with widespread applications in autonomous driving[41], augmented reality[12], and 3D reconstruction[33]. The goal is to predict a dense depth map from a single RGB image. However, performing 3D reconstruction from a single image is an ill-posed problem because perspective projection leads to a loss of one dimension during image formation, and any point along the projection ray may correspond to the same image coordinate. As a result, the distance from the camera to the scene cannot be directly measured from a single view. In the absence of camera calibration parameters, additional sensor measurements (e.g., IMU[49], LiDAR[29]), or strong priors (e.g., pre-trained depth models), a scale ambiguity problem arises. While multiple images (e.g., stereo images or video) can resolve this by localizing points in space, modern large-scale training models typically use data from diverse sources, with significant differences in data types and distributions. These sources include single RGB images, video streams, RGB images without camera calibration, RGB images with sensor parameters, and so on. The differences in these data settings make solving the scale ambiguity problem particularly crucial.

To address the scale ambiguity, one approach is to train on datasets from multiple domains (e.g., indoor and outdoor)[39, 6, 53, 54], learning depth based on the distribution characteristics of the training set. However, biases introduced by these specific datasets can affect the model’s generalization ability, limiting its transferability across domains[36]. Another approach is to find complementary information or constraints shared by these diverse datasets and use this additional information to alleviate the scale ambiguity problem to some extent. Recent works have begun to use language as a supplemental information source, as language has the practical advantage of not requiring additional expensive synchronized and calibrated sensors (e.g., LiDAR, time-of-flight cameras) for data collection. By leveraging existing publicly available pre-trained image description models and vision-language models[38, 20], we can generate textual descriptions for images from different sources and distributions. RSA[59] is a pioneering work in this innovative approach. RSA[59] posits the hypothesis that language (e.g., text descriptions or captions) can be used to infer the scale of 3D scenes, exploring whether linguistic modalities can resolve scale ambiguity in 3D reconstruction from a single image, and successfully converts scale-less relative depth into metrically-scaled depth based on a general relative depth estimation model[39, 6, 53, 54].

However, purely linguistic descriptions suffer from ambiguity. Experiments show that the same image can have multiple descriptions that are semantically similar or even identical. As shown in Figure 1, the RSA[59] estimator produces different estimates for the same image depending on the different textual input. This linguistic ambiguity significantly impacts RSA’s scale recovery. Despite this, language, as an independent input modality distinct from images, is not influenced by factors such as lighting, object orientation, occlusion, or scene layout, making it a highly promising general-purpose tool.

To stabilize the contribution of the linguistic modality, we incorporate high-level semantic information from the corresponding image, extracted via the CLIP Image Encoder[38], alongside the textual description. This approach applies a Visually-Guided mechanism to the linguistic input, effectively mitigating the issue of Linguistic Disambiguation. Our approach, VGLD, also addresses the problem of large differences in depth distributions across different domains (e.g., indoor vs. outdoor). We draw inspiration from ZoeDepth[5] and propose a Domain Router Mechanism (DRM), which automatically determines the domain of the data and routes it to the appropriate estimation head. This mechanism enables automatic routing to the appropriate scope based on domain input and aligns relative depth with metric scale to predict consistent metric depth across domains, achieving

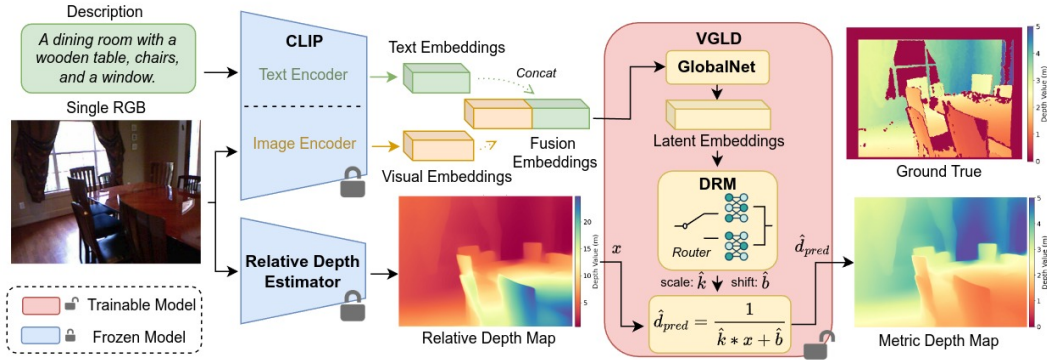


Figure 2: Overview. We infer the scale \hat{k} and shift \hat{b} from the linguistic description and the corresponding image to transform the relative depth from the depth model into a metric depth (absolute depth in meters) prediction.

cross-domain generalization. The scale recovery from relative depth maps to absolute depth maps has multiple recovery paths or ways. To optimize the training trajectory of scalars (scale, shift) parameters, we introduce pseudo-labels (k_{tm}, b_{tm}) obtained from the *Levenberg-Marquardt* algorithm, a nonlinear optimization method that combines gradient descent with the Gauss-Newton method to solve the least squares problem. Through additional supervised training, we effectively guide the model to follow the correct training trajectory, leading to robust depth scale recovery.

Our contributions are as follows: (i) We integrate high-level semantic information from the corresponding image alongside the textual description, thereby stabilizing the output of the scalars parameters; (ii) We introduce the Domain Router Mechanism, which aids in solving the cross-domain estimation problem; (iii) We leverage the Levenberg-Marquardt algorithm to optimize the training trajectory and guide the model’s training process; (iv) We conduct extensive experiments to evaluate the performance of our method in both indoor and outdoor scenarios, analyzing its sensitivity to text captions and its zero-shot generalization capability.

2 Related Work

2.1 Monocular Depth Estimation

Monocular Depth Estimation (MDE) is a fundamental task in computer vision, with its development generally following two main directions: relative depth estimation[39, 40, 60, 6, 53, 54, 21] and metric depth estimation[9, 10, 50, 3, 4, 30, 28, 1, 7, 25, 31, 37, 40, 47, 52, 56, 17, 29]. The goal of metric depth estimation is to predict pixel-wise depth values in metric units (e.g., meters), and models are typically trained by minimizing the discrepancy between predicted and ground-truth depth maps. In contrast, relative depth estimation focuses on inferring the ordinal relationships between pixel pairs, without providing any information about scale or units. A notable early milestone in this field was Eigen *et al.*[9], the first to apply Convolutional Neural Networks (CNNs) to MDE. More recent methods such as AdaBins [3], LocalBins[4] and Binsformer[28] reformulate the depth regression problem as a classification task through depth discretization. Multi-task learning strategies have also been explored: GeoNet[37] integrates surface normal estimation, while AiT[34] incorporates instance segmentation, both to enhance depth prediction through joint training. MiDaS[39, 6] and Diversedepth[55] advances relative depth estimation by pretraining on a diverse mixture of datasets, achieving strong generalization across domains. More recently, Depth Anything[53, 54] unleashes the potential of large-scale unlabeled images and multi-dataset training, substantially improving generalization and robustness across a wide range of scenarios. In addition, diffusion-based[19, 11, 21, 48, 62, 45] methods, such as DDP [19], Marigold [21], and GeoWizard [11], adapt powerful diffusion priors to the depth estimation task via fine-tuning, enabling significant performance gains. Despite these advances, metric depth estimation remains highly domain-sensitive[56], often exhibiting poor robustness when applied to unseen environments. Meanwhile, relative depth estimation, being inherently scale-invariant, cannot be directly used for applications requiring metric 3D reconstruction.

VGLD serves as a universal alignment framework that converts relative depth into consistent metric estimation, enabling robust performance across diverse domains, including both indoor and outdoor scenes.

2.2 Metric Depth Scale Recovery

Relative depth estimation models have emerged as strong backbones for many metric depth Scale Recovery tasks, owing to their impressive cross-domain generalization and robustness. Building on MiDaS[39], DPT[40] replaces the original convolutional architecture with a Vision Transformer and adapts the model to metric depth through fine-tuning on datasets with absolute scale annotations. ZoeDepth[5] adopts MiDaS[39] as the encoder and introduces a powerful decoder equipped with a metric bins module, demonstrating its ability to transfer to metric depth via fine-tuning on metric datasets. Depth Anything[53] further extends ZoeDepth[5] by replacing the MiDaS[39] encoder with its own model, implicitly transforming relative depth into metric depth. Other approaches, such as Metric3D[17, 56], zeroDepth[16] and UniDepth[36], recover metric scale by leveraging or predicting camera intrinsics. PromptDA[29] introduces a low-cost LiDAR sensor as a prompt to guide the Depth Anything[53] model toward accurate metric depth predictions. Despite their progress, these scale recovery methods are typically restricted to specific domains and often require access to ground-truth depth for scale and shift alignment at test time. To address this, RSA[59] introduces a novel approach that explicitly aligns relative depth to metric scale using textual descriptions, enabling cross-domain generalization without requiring ground-truth depth at inference. However, RSA[59] is highly sensitive to textual variation—semantically identical but differently textual descriptions can lead to significant performance degradation. VGLD incorporates high-level semantic features from visual inputs in conjunction with textual descriptions, enabling more robust metric depth scale recovery that is less susceptible to linguistic ambiguity and misalignment.

2.3 Language Modality for Metric Depth Estimation

Recent advances in vision-language models[26, 27, 38, 35, 20], driven by large-scale pretraining across diverse datasets, have led to strong cross-modal representations. These models now serve as effective baselines for various downstream tasks[13, 57, 32, 51, 65] and have been actively explored in monocular depth estimation. DepthCLIP[61] was the first to apply CLIP[38] to this task, reformulating depth regression as a distance classification problem using natural language descriptions such as *"This object is giant, close...far..."*. By leveraging CLIP’s[38] semantic priors, DepthCLIP[61] enables zero-shot depth prediction without additional training by classifying relative distances across image regions. Subsequent works have extended this framework to improve adaptability and performance. Auty *et al.*[2] introduced learnable prompts to replace fixed textual tokens, enhancing the model’s flexibility and effectiveness. Hu *et al.*[18] further proposed a depth codebook with learnable prompts to better handle domain shifts in various scenes. CLIP2Depth[22] introduced mirror embeddings—non-natural language representations—to adapt CLIP[38] for depth estimation while avoiding the need for explicit text prompts. In parallel, methods such as VPD[63], TADP[23], EVP[24] and GeoWizard[11] extract high-level semantics from pretrained text-to-image diffusion models to enhance downstream tasks like depth estimation. Among these, Wordepth[58] was the first to model language as a variational prior for monocular depth estimation. It explicitly encodes object attributes—such as location, size, and orientation—from textual descriptions to align scale-invariant depth predictions with real-world metric scales. Recently, RSA[59] proposed an explicit constraint that enables metric depth recovery from relative estimates by predicting scale directly from textual descriptions. In contrast, VGLD leverages visual features from the CLIP image encoder in conjunction with textual descriptions, yielding more stable scale predictions and improved metric depth estimation over text-only baselines.

3 Method

3.1 Preliminaries

The objective of monocular depth estimation is to predict continuous per-pixel depth values from a single RGB image[9]. We consider a dataset $\mathcal{D} = \{(I^{(n)}, t^{(n)}, d_{gt}^{(n)}, dm_{gt}^{(n)})\}_{n=1}^N$ consisting of N samples, where each sample includes an RGB image $I \in \mathbb{R}^{3 \times H \times W}$, a corresponding linguistic

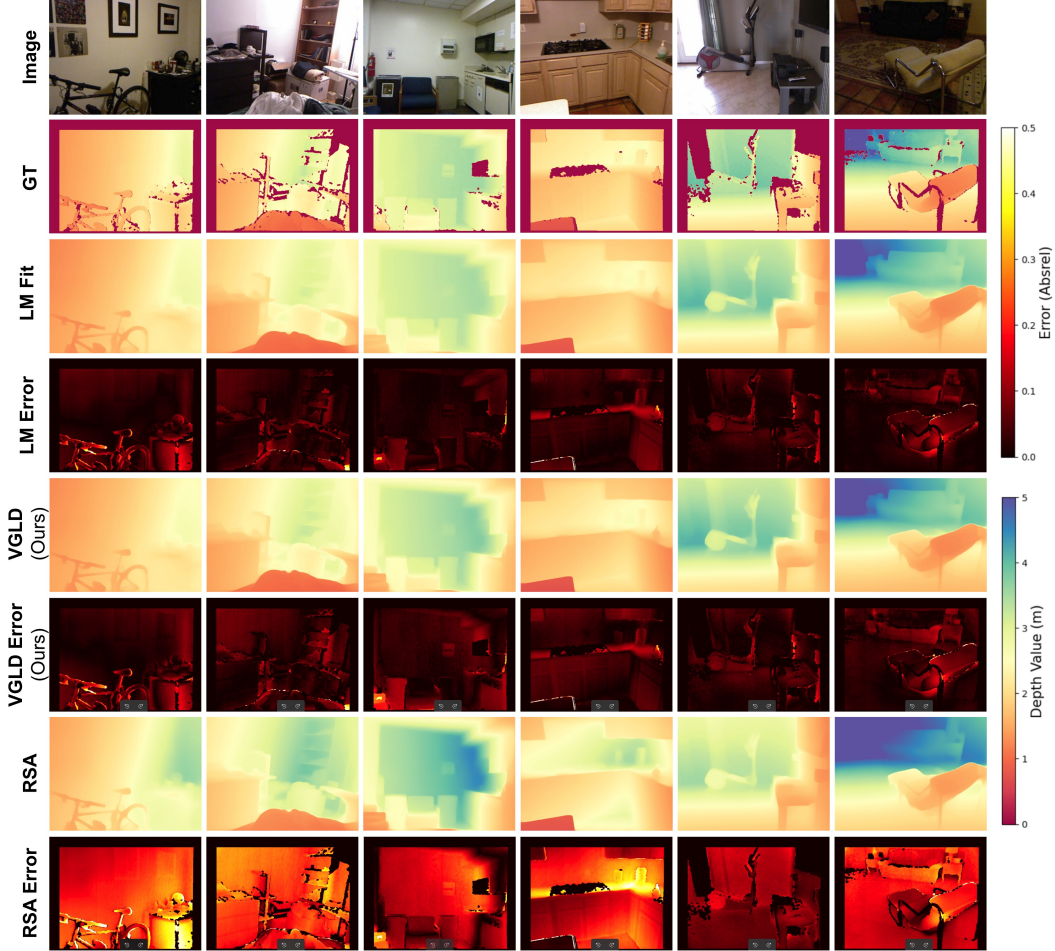


Figure 3: Visualization of depth estimation on the NYUv2 dataset. The LM Fit represents the result obtained using the Levenberg-Marquardt algorithm. Note: Zeros in the ground truth indicate the absence of valid depth values (represented in black or deep red).

description t , a ground-truth metric depth map $d_{gt} \in \mathbb{R}^{H \times W}$ and a ground-truth domain labels $dm_{gt} \in \{0, 1\}$ which represent *indoor* or *outdoor* scene. We build upon a pretrained monocular relative depth estimation model h_θ , which serves as the foundation for our metric depth scale recovery framework. Given an RGB image, the model predicts an inverse relative depth map $x \in \mathbb{R}^{H \times W}$, which lacks absolute scale information. To recover metric-scale depth from this scaleless prediction, we apply a global linear transformation informed by both the linguistic description and high-level visual semantics of the image. Specifically, similar to RSA[59], we predict a pair of scalars $(\hat{k}, \hat{b}) \in \mathbb{R}^2$ that represent the scale and shift parameters of the transformation. The final metric depth prediction is then computed as:

$$\hat{d}_{pred} = \frac{1}{\hat{k} \cdot x + \hat{b}}, \text{ where } \hat{d}_{pred} \in \mathbb{R}^{H \times W} \quad (1)$$

3.2 VGLD

To model the relationship between the linear transformation parameters and the semantic content of both the image and its linguistic description, we leverage the CLIP model as a feature extractor. Benefiting from large-scale contrastive pretraining[38], CLIP provides a shared latent space that is well-suited for aligning object-centric visual and linguistic representations. Given an input sample $\{I, t\}$, we first extract visual and text embeddings using the CLIP image encoder and CLIP text encoder, respectively. The resulting embeddings are concatenated to form a fused representation,

which is subsequently passed through a lightweight encoder network, GlobalNet—a three-layer MLP—to produce a compact 256-dimensional latent embedding used for downstream scale parameter regression.

Following ZoeDepth[5], we employ a lightweight MLP-based classifier, referred to as the Domain Routing Mechanism (**DRM**), to predict the domain of the input image based on its latent embedding. We consider two domains: indoor and outdoor. The predicted domain is then used to route the latent embedding to the corresponding domain-specific scalars prediction head.

3.3 Loss Function

As illustrated in Figure 2, the VGLD model freezes the weights of both the CLIP backbone and the relative depth estimator during training, and updates only the parameters of the GlobalNet and DRM modules. These modules are jointly optimized under a unified loss function. Since VGLD focuses on predicting a pair of global scalars rather than pixel-wise metric depth values, we do not adopt the Scale-Invariant Logarithmic Loss, which is more suitable for dense depth estimation tasks. Instead, following RSA[59], we adopt the L1 loss, which provides a more direct and interpretable supervision signal for scalars regression. The \mathcal{L}_{metric} is formulated as:

$$\mathcal{L}_{metric} = \frac{1}{M} \sum_{(i,j) \in \Omega} m(i,j) \times |\hat{d}_{pred}(i,j) - d_{gt}(i,j)|, \quad (2)$$

where \hat{d}_{pred} denotes the predicted metric depth, $(i,j) \in \Omega$ represents the image coordinates, $m(\cdot) \in \{0,1\}$ denotes the binary mask map and M represents the number of pixels with valid ground truth values. We introduce a domain classification loss, denoted as \mathcal{L}_{dm} , implemented using the cross-entropy loss:

$$\mathcal{L}_{domain} = CrossEntropy(\hat{dm}_{pred}, dm_{gt}) \quad (3)$$

where $\hat{dm}_{pred} \in \{0,1\}$ is the predicted domain label, and $dm_{gt} \in \{0,1\}$ is the corresponding ground-truth domain. To guide the model towards the optimal solution, we employ an MSE loss to provide LM loss (scalars supervision) for the modules:

$$\mathcal{L}_{lm} = 10 \times (\hat{k} - k_{lm})^2 + (\hat{b} - b_{lm})^2 \quad (4)$$

where (\hat{k}, \hat{b}) are the predicted LM scalars from VGLD, and (k_{lm}, b_{lm}) are the corresponding pseudo-labels provided by the Levenberg-Marquardt algorithm. The total loss is defined as follows:

$$\mathcal{L}_{total} = \mathcal{L}_{metric} + \alpha \times \mathcal{L}_{domain} + \beta \times \mathcal{L}_{lm} \quad (5)$$

In our experiments, we set α and β to 0.1, as is customary.

4 Experiments

4.1 Experimental Settings

Dataset. We primarily train on two datasets: NYUv2[43] and KITTI[14], representing indoor and outdoor scenes, respectively. NYUv2 contains images with a resolution of 480x640, with depth values ranging from 0 to 10 meters. In accordance with the official dataset split[25], we use 24,231 image-depth pairs for training and 654 image-depth pairs for testing. KITTI is an outdoor dataset collected from equipment mounted on a moving vehicle, with depth values ranging from 0 to 80 meters. Following KBCrop[46], all RGB images and depth maps are cropped to a resolution of 1216x352. We adopt the Eigen split[9], which includes 23,158 training images and 652 test images, to train and evaluate our method. Additionally, we report zero-shot generalization results on SUN-RGBD[44], which includes 5,050 test images, DIML Indoor[8], which contains 503 validation images and DDAD[15], which contains 3950 validation images.

Relative Depth Models. We use MiDaS 3.1[6] with the dpt_swin2_large_384 model (213M parameters), MiDaS 3.0[39] with the dpt_large_384 model (123M parameters), DepthAnything[53] with DepthAnything-Small model (24.8M parameters), and DepthAnything v2[54] with DepthAnything-V2-Small model (24.8M parameters). Additionally, we apply the Least Squares and Levenberg-Marquardt algorithms, which predict a global scale and offset based on the corresponding ground-truth depth maps, scaling relative depth accordingly, as detailed in Tables 1, 2, 7, 8.

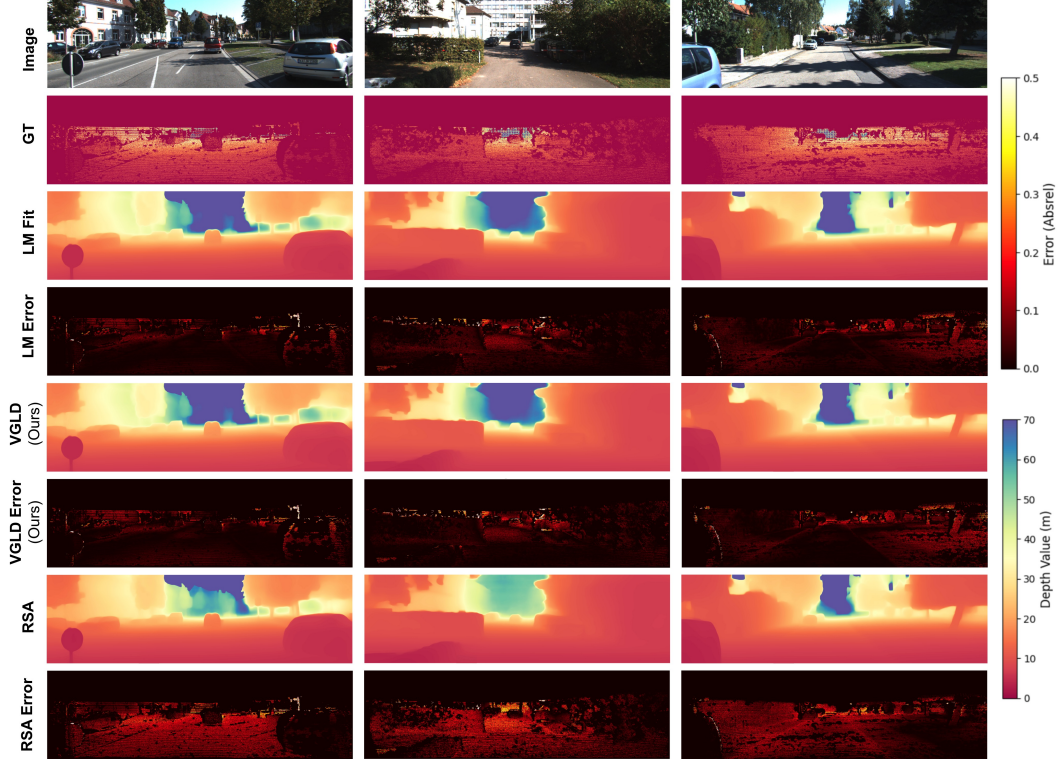


Figure 4: Visualization of depth estimation on the KITTI dataset. The LM Fit represents the result obtained using the Levenberg-Marquardt algorithm. Note: Zeros in the ground truth indicate the absence of valid depth values (represented in black or deep red).

The Proposed Models. For clarity, we denote the proposed models as VGLD- $\{\text{dataset}\}$ - $\{\text{method}\}$. The dataset refers to the training datasets, which include "N" for NYUv2, "K" for KITTI, and "NK" for both NYUv2 and KITTI. The method refers to the type of embeddings used: "T" for text embeddings only, "I" for visual embeddings only, and "TCI" for both text and visual embeddings (i.e., Fusion Embeddings, as shown in Figure 2).

Training details. The proposed VGLD is implemented in PyTorch. We use the Adam optimizer with parameters $(\beta_1, \beta_2, wd) = (0.9, 0.999, 0.001)$ and a learning rate of 3×10^{-4} . All models are trained for 24 epochs on a single NVIDIA RTX 3090 GPU with 24GB of memory. The batch size is set to 6, and the total training time for each model is approximately 19 to 22 hours.

Evaluation details. We evaluate performance using several metrics, including mean absolute relative error (Abs Rel), squared relative error (sq_rel), root mean square error (RMSE), root mean square error in log space (RMSE_{log}), absolute error in log space (log₁₀) and threshold accuracy (δ_i).

4.2 Experimental Results

Quantitative results. We present the results on NYUv2 in Table 1 and on KITTI in Table 2. Our approach surpasses RSA[59] in all evaluation metrics and achieves performance close to that of scaling with ground-truth values, as highlighted in yellow in the all quantitative tables. Following [39], we perform linear regression to find the scale and shift that minimize the least-squares error between the ground-truth and predicted metric depth. Additionally, we employ the Levenberg-Marquardt algorithm for more accurate nonlinear fitting. We trained separate VGLD models for each dataset and also a unified VGLD model combining NYUv2 and KITTI, denoted as VGLD-NK- $\{\text{method}\}$. The VGLD model trained on a single dataset shows slightly better performance compared to the unified model, benefiting from the precise routing functionality of the DRM module, the performance gap between the single-dataset and unified models is minimal. Furthermore, VGLD models using visual embeddings (VGLD- $\{\text{dataset}\}$ -I) consistently outperform those using only text embeddings (VGLD-

RDE Model‡	Method	Lower is better					Higher is better		
		Abs Rel ↓	sq_rel ↓	RMSE ↓	RMSE _{log} ↓	log ₁₀ ↓	D1 ↑	D2 ↑	D3 ↑
ZoeDepth[5]	robust depth estimation †	0.077	–	0.277	–	0.033	0.953	0.995	0.999
ZeroDepth[16]		0.074	–	0.269	–	0.103	0.954	0.995	1.000
Metric3Dv2[17]		0.047	–	0.183	–	0.020	0.989	0.998	1.000
	Least Squares	0.121	0.073	0.388	0.338	0.068	0.866	0.959	0.978
	Levenberg Marquardt	0.056	0.021	0.218	0.080	0.024	0.969	0.995	0.998
MiDas-1[6]	RSA-N[59]	0.171	–	0.569	–	0.072	0.731	0.955	0.993
	RSA-NK[59]	0.168	–	0.561	–	0.071	0.737	0.959	0.993
	VGLD-N-T (Ours)	0.158	0.113	0.529	0.181	0.068	0.758	0.965	0.994
	VGLD-N-I (Ours)	0.121	<u>0.068</u>	<u>0.423</u>	0.146	0.053	0.860	0.985	0.998
	VGLD-N-TCI (Ours)	0.119	0.067	0.414	0.142	0.051	0.867	<u>0.984</u>	0.998
	VGLD-NK-T (Ours)	0.159	0.113	0.526	0.178	0.067	0.751	0.971	<u>0.995</u>
	VGLD-NK-I (Ours)	0.123	0.070	0.426	0.147	0.053	0.855	0.982	0.998
	VGLD-NK-TCI (Ours)	<u>0.120</u>	<u>0.068</u>	0.414	<u>0.143</u>	<u>0.052</u>	<u>0.863</u>	<u>0.984</u>	0.998
MiDas-2[39]	Least Squares	0.130	0.085	0.421	0.286	0.066	0.845	0.956	0.980
	Levenberg Marquardt	0.094	0.049	0.330	0.122	0.039	0.916	0.985	0.997
	VGLD-N-T (Ours)	0.180	0.140	0.596	0.212	0.078	0.688	0.946	0.990
	VGLD-N-I (Ours)	<u>0.154</u>	<u>0.106</u>	0.524	0.186	0.067	0.775	0.960	0.993
	VGLD-N-TCI (Ours)	0.151	0.104	0.507	0.181	0.064	0.789	0.964	0.993
	VGLD-NK-T (Ours)	0.182	0.147	0.615	0.217	0.080	0.682	0.939	0.989
	VGLD-NK-I (Ours)	0.155	0.108	0.520	0.185	0.066	0.776	<u>0.961</u>	<u>0.992</u>
	VGLD-NK-TCI (Ours)	0.151	0.104	<u>0.513</u>	<u>0.183</u>	<u>0.065</u>	<u>0.780</u>	0.964	0.993
DAV2-vits[54]	Least Squares	0.122	0.074	0.392	0.362	0.070	0.866	0.959	0.977
	Levenberg Marquardt	0.052	0.021	0.209	0.077	0.022	0.969	0.992	0.998
	VGLD-N-T (Ours)	0.163	0.119	0.546	0.191	0.073	0.713	0.964	<u>0.994</u>
	VGLD-N-I (Ours)	0.128	<u>0.074</u>	<u>0.433</u>	0.154	<u>0.057</u>	<u>0.830</u>	<u>0.983</u>	0.995
	VGLD-N-TCI (Ours)	0.125	0.073	0.423	0.152	0.055	0.842	0.984	0.995
	VGLD-NK-T (Ours)	0.161	0.115	0.539	0.189	0.073	0.714	0.967	<u>0.994</u>
	VGLD-NK-I (Ours)	<u>0.127</u>	<u>0.074</u>	0.436	<u>0.155</u>	<u>0.057</u>	0.835	0.982	0.995
	VGLD-NK-TCI (Ours)	<u>0.127</u>	<u>0.074</u>	0.434	<u>0.155</u>	<u>0.057</u>	0.835	0.981	0.995
DAV1-vits[53]	Least Squares	0.121	0.075	0.397	0.327	0.067	0.863	0.959	0.979
	Levenberg Marquardt	0.057	0.022	0.230	0.081	0.024	0.967	0.995	0.999
	RSA-N[59]	0.147	–	0.484	–	0.065	0.775	0.975	0.997
	RSA-NK[59]	0.148	–	0.498	–	0.065	0.776	0.974	0.996
	VGLD-N-T (Ours)	0.145	0.094	0.496	0.170	0.064	0.792	0.974	0.997
	VGLD-N-I (Ours)	0.115	0.061	0.405	0.141	0.051	0.872	<u>0.987</u>	<u>0.998</u>
	VGLD-N-TCI (Ours)	0.112	0.058	0.390	0.135	<u>0.049</u>	0.887	0.988	<u>0.998</u>
	VGLD-NK-T (Ours)	0.142	0.089	0.483	0.168	0.063	0.787	0.979	0.997
	VGLD-NK-I (Ours)	<u>0.114</u>	0.061	0.404	<u>0.138</u>	0.050	0.880	<u>0.987</u>	0.999
	VGLD-NK-TCI (Ours)	0.112	<u>0.059</u>	<u>0.392</u>	0.135	0.048	<u>0.883</u>	0.988	0.999

Table 1: Quantitative Depth Comparison on the NYUV2 Dataset. The yellow regions represent the results obtained using least-squares-type mathematical fitting methods. † denotes the results of certain state-of-the-art (SOTA) absolute scale estimation models. ‡ In the RDE Model column, MiDas-1 refers to the model using Midas-V3.1-dpt_swin2_large_384, MiDas-2 refers to the model using Midas-V3.0-dpt_large_384, DAV2-vits refers to the model using Depth-Anything-V2-Small, and DAV1-vits refers to the model using Depth-Anything-V1-Small. Best results are in **bold**, second best are underlined.

{dataset}-T), validating the effectiveness of using visual rather than purely linguistic cues for scale prediction. Building on this, we combine both visual and text embeddings (VGLD-{dataset}-TCI), enabling visual embeddings to guide text semantic alignment and addressing the visually-guided linguistic disambiguation problem.

Qualitative comparisons. We present comparison examples of VGLD and baseline methods on the NYUv2 and KITTI datasets in Figures 1 and 2, respectively. The error maps display the absolute relative error, where the overall brightness of the error maps clearly indicates the performance of our method. Notably, our approach achieves performance very close to that of the Levenberg-Marquardt fitting (LM Fit) across different scenes, demonstrating robust metric depth scale recovery. In contrast to the fixed scale and shift estimates produced by RSA, VGLD significantly improves the accuracy of depth predictions, with darker error maps indicating reduced error. Note: All qualitative comparison results in the VGLD section are inferred from the VGLD-NK-TCI method, where the RDE model used is DAV1-vits.

Sensitivity to Variations in Linguistic Descriptions. A single image can be described using multiple textual expressions. To investigate how linguistic variation affects metric depth scale recovery, we evaluate the influence of different textual inputs on VGLD’s performance. We observe that while

RDE Model	Method	Lower is better					Higher is better		
		Abs Rel ↓	sq_rel ↓	RMSE ↓	RMSE _{log} ↓	log ₁₀ ↓	D1 ↑	D2 ↑	D3 ↑
ZoeDepth[5]	robust depth estimation	0.054	–	2.281	0.082	–	0.971	0.996	0.999
ZeroDepth[16]		0.053	–	2.087	0.083	–	0.968	0.995	0.999
Metric3Dv2[17]		0.044	–	1.985	0.064	–	0.985	0.998	0.999
	Least Squares	0.333	2.094	6.901	1.731	0.293	0.408	0.790	0.879
	Levenberg Marquardt	0.091	0.425	3.373	0.127	0.038	0.925	0.987	0.996
MiDas-1[6]	RSA-K[59]	0.163	–	4.082	0.185	–	0.798	0.948	0.981
	RSA-NK[59]	0.160	–	4.232	0.194	–	0.782	0.946	0.980
	VGLD-K-T(Ours)	0.133	0.608	3.755	0.162	<u>0.056</u>	0.854	0.975	0.993
	VGLD-K-I(Ours)	0.120	0.526	3.668	0.152	0.051	0.868	<u>0.979</u>	<u>0.995</u>
	VGLD-K-TCI(Ours)	0.120	0.523	3.598	<u>0.151</u>	0.051	<u>0.871</u>	0.980	0.996
	VGLD-NK-T(Ours)	0.130	0.568	3.744	0.161	<u>0.056</u>	0.844	0.975	<u>0.995</u>
	VGLD-NK-I(Ours)	<u>0.122</u>	0.543	<u>3.574</u>	<u>0.151</u>	0.051	0.868	<u>0.979</u>	<u>0.995</u>
	VGLD-NK-TCI(Ours)	0.120	<u>0.528</u>	3.559	0.150	0.051	0.874	0.980	0.996
MiDas-2[39]	Least Squares	0.336	2.172	6.925	1.658	0.283	0.421	0.778	0.876
	Levenberg Marquardt	0.155	0.770	4.190	0.185	0.062	0.809	0.966	0.990
	VGLD-K-T(Ours)	0.194	1.290	5.030	0.225	0.079	0.709	0.930	0.981
	VGLD-K-I(Ours)	0.183	1.154	4.842	0.215	0.075	0.733	<u>0.942</u>	<u>0.983</u>
	VGLD-K-TCI(Ours)	0.178	1.146	<u>4.806</u>	0.210	0.073	0.748	<u>0.942</u>	0.984
	VGLD-NK-T(Ours)	0.191	1.260	4.994	0.221	0.078	0.723	0.932	0.981
	VGLD-NK-I(Ours)	0.184	1.179	4.808	0.213	<u>0.074</u>	<u>0.740</u>	0.938	0.984
	VGLD-NK-TCI(Ours)	<u>0.180</u>	<u>1.158</u>	4.804	<u>0.212</u>	<u>0.074</u>	0.737	0.943	0.984
DAV2-vits[54]	Least Squares	0.330	2.053	6.737	1.729	0.292	0.423	0.790	0.877
	Levenberg Marquardt	0.103	0.454	3.277	0.135	0.042	0.919	0.987	0.997
	VGLD-K-T(Ours)	0.166	0.822	4.189	0.190	0.070	0.756	0.953	0.992
	VGLD-K-I(Ours)	0.154	0.698	4.219	0.187	0.067	0.756	0.966	<u>0.995</u>
	VGLD-K-TCI(Ours)	0.152	0.657	3.872	0.179	0.065	0.779	<u>0.972</u>	0.996
	VGLD-NK-T(Ours)	0.164	0.786	4.287	0.193	0.070	0.752	0.955	0.993
	VGLD-NK-I(Ours)	0.160	0.748	4.031	0.187	0.069	0.761	0.965	<u>0.995</u>
	VGLD-NK-TCI(Ours)	<u>0.153</u>	<u>0.695</u>	<u>3.980</u>	<u>0.180</u>	<u>0.066</u>	<u>0.772</u>	0.973	0.996
DAV1-vits[53]	Least Squares	0.331	2.078	6.772	1.714	0.291	0.423	0.786	0.875
	Levenberg Marquardt	0.112	0.495	3.375	0.142	0.045	0.897	0.986	0.997
	RSA-K[59]	0.160	–	4.437	0.189	–	0.780	0.958	0.988
	RSA-NK[59]	0.158	–	4.457	0.179	–	0.786	0.967	0.987
	VGLD-K-T(Ours)	0.151	0.747	4.354	0.186	0.066	0.773	0.963	0.994
	VGLD-K-I(Ours)	0.144	<u>0.646</u>	<u>4.074</u>	0.178	0.063	0.790	<u>0.975</u>	<u>0.996</u>
	VGLD-K-TCI(Ours)	<u>0.140</u>	0.686	4.081	<u>0.172</u>	<u>0.061</u>	0.807	<u>0.975</u>	<u>0.996</u>
	VGLD-NK-T(Ours)	0.148	0.728	4.293	0.183	0.065	0.781	0.966	0.995
VGLD-NK-I(Ours)	0.142	0.759	4.151	<u>0.172</u>	<u>0.061</u>	<u>0.814</u>	<u>0.975</u>	<u>0.996</u>	
VGLD-NK-TCI(Ours)	0.136	0.632	4.008	0.169	0.059	0.816	0.977	0.997	

Table 2: Quantitative Depth Comparison on the KITTI Dataset. The yellow regions represent the results obtained using least-squares-type mathematical fitting methods. Best results are in **bold**, second best are underlined.

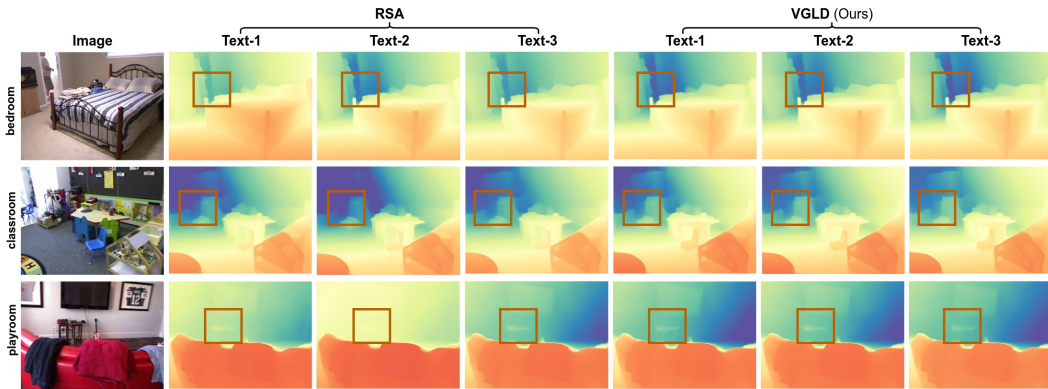


Figure 5: Sensitivity to variations in linguistic descriptions on the NYUv2 dataset. Depth maps show that the RSA method is susceptible to different textual inputs, resulting in inconsistent estimations, especially in the regions highlighted by orange boxes. In contrast, our VGLD method yields more stable predictions. Warmer colors (red) indicate closer distances, while cooler colors (blue) indicate farther distances.

the RSA method—relying solely on textual descriptions—is highly sensitive to phrasing, VGLD exhibits significantly greater robustness, consistently producing stable predictions for scale and shift. Moreover, VGLD often outperforms RSA across evaluation metrics, highlighting its ability to provide reliable scalars estimations. Figures 5 and 6 present qualitative comparisons on NYU and KITTI under three distinct text prompts. The corresponding quantitative results are provided in Tables 3 and 4, while Tables 5 and 6 list the three textual descriptions used for each image, as detailed in the Supplementary Material (Section 7)..

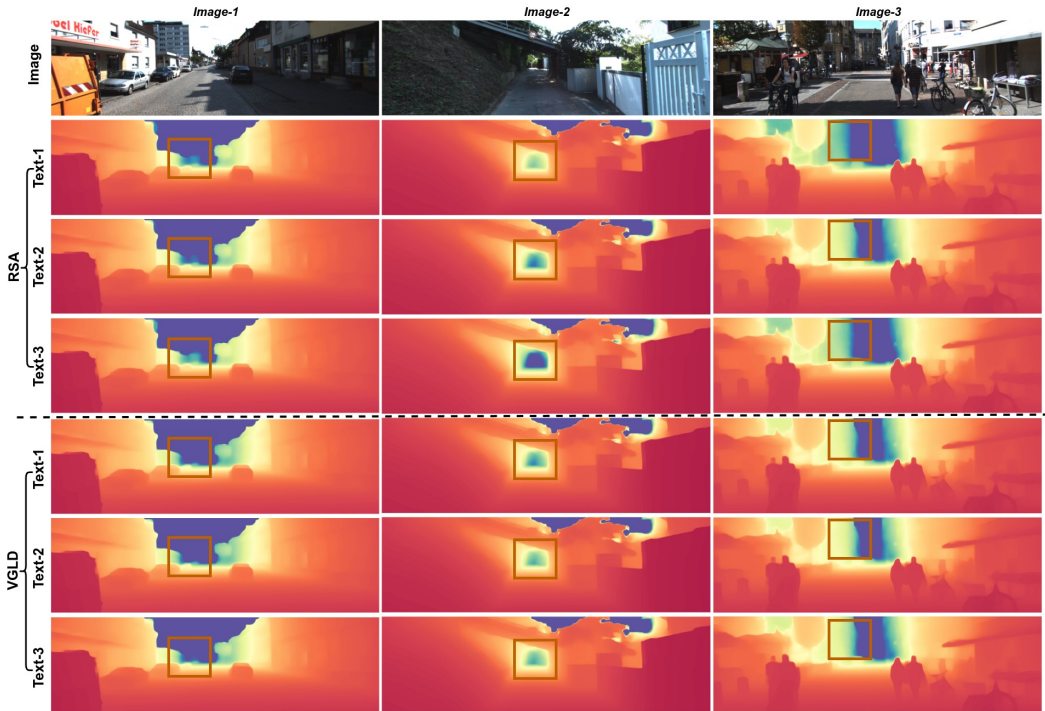


Figure 6: Sensitivity to variations in linguistic descriptions on the KITTI dataset. Depth maps show that the RSA method is susceptible to different textual inputs, resulting in inconsistent estimations, especially in the regions highlighted by orange boxes. In contrast, our VGLD method yields more stable predictions. Warmer colors (red) indicate closer distances, while cooler colors (blue) indicate farther distances.

5 Conclusion

We propose an enhanced framework, VGLD, that leverages linguistic descriptions as input and utilizes high-level semantic information from images to address the issue of linguistic ambiguity. VGLD effectively harnesses pre-trained CLIP Text Encoder and Image Encoder to extract rich semantic information from both text and images, and jointly employs these features through an MLP-based model to map them into shift and scale parameters, robustly converting relative depth maps into metric-depth predictions. Extensive experiments on indoor and outdoor benchmark datasets, along with four pre-trained relative depth models, demonstrate VGLD’s strong robustness, validating that vision can correctly guide language and resolve textual ambiguities during inference, enabling accurate depth scale recovery without ground truth values. We also present a unified model, VGLD-NK-{method}, which is trained across both indoor and outdoor datasets. Thanks to the design of the Domain Router Mechanism (DRM), the VGLD model can easily generalize across different scene compositions, highlighting the importance of the DRM module. Finally, a zero-shot generalization experiment shows that, even on unseen data domains, VGLD can effectively guide linguistic inputs without additional training. While the linguistic modality is invariant to common visual variations, the sole reliance on language modalities can still struggle to fully and accurately describe a specific image. In comparison to additional modalities (e.g., IMU, LiDAR sensors), using the image modality to complement the required semantic information for the task is a convenient and effective approach.

5.1 Limitations and future work.

Although linguistic-based scale recovery under visually-guided methods is highly robust, VGLD is still influenced by language modality. For different descriptions of the same image, the VGLD model may output inconsistent results (albeit with small error margins), especially when incorrect descriptions are used (e.g., describing an indoor scene as "a photo of a narrow street."). To address this issue, one feasible approach could be to further match the similarity between the language and image modalities, effectively excluding erroneous image descriptions. Future work could expand the image modality-assisted features of VGLD to enable more robust and fine-grained scale estimation, as well as enhance the model's ability to handle malicious attacks in text descriptions.

References

- [1] A. Agarwal and C. Arora. Attention attention everywhere: Monocular depth prediction with skip attention. In *Proceedings of the IEEE/CVF Winter Conference on Applications of Computer Vision*, pages 5861–5870, 2023.
- [2] D. Auty and K. Mikolajczyk. Learning to prompt clip for monocular depth estimation: Exploring the limits of human language. In *Proceedings of the IEEE/CVF International Conference on Computer Vision*, pages 2039–2047, 2023.
- [3] S. F. Bhat, I. Alhashim, and P. Wonka. Adabins: Depth estimation using adaptive bins. In *Proceedings of the IEEE/CVF conference on computer vision and pattern recognition*, pages 4009–4018, 2021.
- [4] S. F. Bhat, I. Alhashim, and P. Wonka. Localbins: Improving depth estimation by learning local distributions. In *European Conference on Computer Vision*, pages 480–496. Springer, 2022.
- [5] S. F. Bhat, R. Birkl, D. Wofk, P. Wonka, and M. Müller. Zoedepth: Zero-shot transfer by combining relative and metric depth. In *arXiv preprint arXiv:2302.12288*, 2023.
- [6] R. Birkl, D. Wofk, and M. Müller. Midas v3. 1—a model zoo for robust monocular relative depth estimation. In *arXiv preprint arXiv:2307.14460*, 2023.
- [7] W. Chang, Y. Zhang, and Z. Xiong. Transformer-based monocular depth estimation with attention supervision. In *BMVC*, volume 6, page 7, 2021.
- [8] J. Cho, D. Min, Y. Kim, and K. Sohn. Diml/cvl rgb-d dataset: 2m rgb-d images of natural indoor and outdoor scenes. In *arXiv preprint arXiv:2110.11590*, 2021.
- [9] D. Eigen, C. Puhrsch, and R. Fergus. Depth map prediction from a single image using a multi-scale deep network. In *Advances in neural information processing systems*, volume 27, 2014.
- [10] H. Fu, M. Gong, C. Wang, K. Batmanghelich, and D. Tao. Deep ordinal regression network for monocular depth estimation. In *Proceedings of the IEEE conference on computer vision and pattern recognition*, pages 2002–2011, 2018.
- [11] X. Fu, W. Yin, M. Hu, K. Wang, Y. Ma, P. Tan, S. Shen, D. Lin, and X. Long. Geowizard: Unleashing the diffusion priors for 3d geometry estimation from a single image. In *European Conference on Computer Vision*, pages 241–258. Springer, 2024.
- [12] A. Ganj, Y. Zhao, H. Su, and T. Guo. Mobile ar depth estimation: Challenges & prospects—extended version. In *arXiv preprint arXiv:2310.14437*, 2023.
- [13] P. Gao, S. Geng, R. Zhang, T. Ma, R. Fang, Y. Zhang, H. Li, and Y. Qiao. Clip-adapter: Better vision-language models with feature adapters. In *International booktitle of Computer Vision*, volume 132, pages 581–595. Springer, 2024.
- [14] A. Geiger, P. Lenz, and R. Urtasun. Are we ready for autonomous driving. In *The KITTI vision benchmark suite. In CVPR*, volume 2, page 5, 2012.

- [15] V. Guizilini, R. Ambrus, S. Pillai, A. Raventos, and A. Gaidon. 3d packing for self-supervised monocular depth estimation. In *Proceedings of the IEEE/CVF conference on computer vision and pattern recognition*, pages 2485–2494, 2020.
- [16] V. Guizilini, I. Vasiljevic, D. Chen, R. Ambrus, and A. Gaidon. Towards zero-shot scale-aware monocular depth estimation. In *Proceedings of the IEEE/CVF International Conference on Computer Vision*, pages 9233–9243, 2023.
- [17] M. Hu, W. Yin, C. Zhang, Z. Cai, X. Long, H. Chen, K. Wang, G. Yu, C. Shen, and S. Shen. Metric3d v2: A versatile monocular geometric foundation model for zero-shot metric depth and surface normal estimation. In *arXiv preprint arXiv:2404.15506*, 2024.
- [18] X. Hu, C. Zhang, Y. Zhang, B. Hai, K. Yu, and Z. He. Learning to adapt clip for few-shot monocular depth estimation. In *Proceedings of the IEEE/CVF Winter Conference on Applications of Computer Vision*, pages 5594–5603, 2024.
- [19] Y. Ji, Z. Chen, E. Xie, L. Hong, X. Liu, Z. Liu, T. Lu, Z. Li, and P. Luo. Ddp: Diffusion model for dense visual prediction. In *Proceedings of the IEEE/CVF International Conference on Computer Vision*, pages 21741–21752, 2023.
- [20] M. Jia, L. Tang, B.-C. Chen, C. Cardie, S. Belongie, B. Hariharan, and S.-N. Lim. Visual prompt tuning. In *European conference on computer vision*, pages 709–727. Springer, 2022.
- [21] B. Ke, A. Obukhov, S. Huang, N. Metzger, R. C. Daudt, and K. Schindler. Repurposing diffusion-based image generators for monocular depth estimation. In *Proceedings of the IEEE/CVF Conference on Computer Vision and Pattern Recognition*, pages 9492–9502, 2024.
- [22] D. Kim and S. Lee. Clip can understand depth. In *arXiv preprint arXiv:2402.03251*, 2024.
- [23] N. Kondapaneni, M. Marks, M. Knott, R. Guimaraes, and P. Perona. Text-image alignment for diffusion-based perception. In *Proceedings of the IEEE/CVF Conference on Computer Vision and Pattern Recognition*, pages 13883–13893, 2024.
- [24] M. Lavreniuk, S. F. Bhat, M. Müller, and P. Wonka. Evp: Enhanced visual perception using inverse multi-attentive feature refinement and regularized image-text alignment. In *arXiv preprint arXiv:2312.08548*, 2023.
- [25] J. H. Lee, M.-K. Han, D. W. Ko, and I. H. Suh. From big to small: Multi-scale local planar guidance for monocular depth estimation. In *arXiv preprint arXiv:1907.10326*, 2019.
- [26] J. Li, D. Li, C. Xiong, and S. Hoi. Blip: Bootstrapping language-image pre-training for unified vision-language understanding and generation. In *International conference on machine learning*, pages 12888–12900. PMLR, 2022.
- [27] J. Li, D. Li, S. Savarese, and S. Hoi. Blip-2: Bootstrapping language-image pre-training with frozen image encoders and large language models. In *International conference on machine learning*, pages 19730–19742. PMLR, 2023.
- [28] Z. Li, X. Wang, X. Liu, and J. Jiang. Binsformer: Revisiting adaptive bins for monocular depth estimation. In *IEEE Transactions on Image Processing*. IEEE, 2024.
- [29] H. Lin, S. Peng, J. Chen, S. Peng, J. Sun, M. Liu, H. Bao, J. Feng, X. Zhou, and B. Kang. Prompting depth anything for 4k resolution accurate metric depth estimation. In *arXiv preprint arXiv:2412.14015*, 2024.
- [30] C. Liu, S. Kumar, S. Gu, R. Timofte, and L. Van Gool. Va-depthnet: A variational approach to single image depth prediction. In *arXiv preprint arXiv:2302.06556*, 2023.
- [31] X. Long, C. Lin, L. Liu, W. Li, C. Theobalt, R. Yang, and W. Wang. Adaptive surface normal constraint for depth estimation. In *Proceedings of the IEEE/CVF international conference on computer vision*, pages 12849–12858, 2021.
- [32] T. Lüddecke and A. Ecker. Image segmentation using text and image prompts. In *Proceedings of the IEEE/CVF conference on computer vision and pattern recognition*, pages 7086–7096, 2022.

- [33] L. Mescheder, M. Oechsle, M. Niemeyer, S. Nowozin, and A. Geiger. Occupancy networks: Learning 3d reconstruction in function space. In *Proceedings of the IEEE/CVF conference on computer vision and pattern recognition*, pages 4460–4470, 2019.
- [34] J. Ning, C. Li, Z. Zhang, C. Wang, Z. Geng, Q. Dai, K. He, and H. Hu. All in tokens: Unifying output space of visual tasks via soft token. In *Proceedings of the IEEE/CVF International Conference on Computer Vision*, pages 19900–19910, 2023.
- [35] M. Oquab, T. Darcet, T. Moutakanni, H. Vo, M. Szafraniec, V. Khalidov, P. Fernandez, D. Haziza, F. Massa, A. El-Nouby, et al. Dinov2: Learning robust visual features without supervision. In *arXiv preprint arXiv:2304.07193*, 2023.
- [36] L. Piccinelli, Y.-H. Yang, C. Sakaridis, M. Segu, S. Li, L. Van Gool, and F. Yu. Unidepth: Universal monocular metric depth estimation. In *Proceedings of the IEEE/CVF Conference on Computer Vision and Pattern Recognition*, pages 10106–10116, 2024.
- [37] X. Qi, R. Liao, Z. Liu, R. Urtasun, and J. Jia. Geonet: Geometric neural network for joint depth and surface normal estimation. In *Proceedings of the IEEE Conference on Computer Vision and Pattern Recognition*, pages 283–291, 2018.
- [38] A. Radford, J. W. Kim, C. Hallacy, A. Ramesh, G. Goh, S. Agarwal, G. Sastry, A. Askell, P. Mishkin, J. Clark, et al. Learning transferable visual models from natural language supervision. In *International conference on machine learning*, pages 8748–8763. PMLR, 2021.
- [39] R. Ranftl, K. Lasinger, D. Hafner, K. Schindler, and V. Koltun. Towards robust monocular depth estimation: Mixing datasets for zero-shot cross-dataset transfer. In *IEEE transactions on pattern analysis and machine intelligence*, volume 44, pages 1623–1637. IEEE, 2020.
- [40] R. Ranftl, A. Bochkovskiy, and V. Koltun. Vision transformers for dense prediction. In *Proceedings of the IEEE/CVF international conference on computer vision*, pages 12179–12188, 2021.
- [41] M. Schön, M. Buchholz, and K. Dietmayer. Mgnet: Monocular geometric scene understanding for autonomous driving. In *Proceedings of the IEEE/CVF International Conference on Computer Vision*, pages 15804–15815, 2021.
- [42] S. Shao, Z. Pei, W. Chen, R. Li, Z. Liu, and Z. Li. Urcdc-depth: Uncertainty rectified cross-distillation with cutflip for monocular depth estimation. In *IEEE Transactions on Multimedia*. IEEE, 2023.
- [43] N. Silberman, D. Hoiem, P. Kohli, and R. Fergus. Indoor segmentation and support inference from rgb-d images. In *Computer Vision—ECCV 2012: 12th European Conference on Computer Vision, Florence, Italy, October 7–13, 2012, Proceedings, Part V 12*, pages 746–760. Springer, 2012.
- [44] S. Song, S. P. Lichtenberg, and J. Xiao. Sun rgb-d: A rgb-d scene understanding benchmark suite. In *Proceedings of the IEEE conference on computer vision and pattern recognition*, pages 567–576, 2015.
- [45] Z. Song, Z. Wang, B. Li, H. Zhang, R. Zhu, L. Liu, P.-T. Jiang, and T. Zhang. Depthmaster: Taming diffusion models for monocular depth estimation. In *arXiv preprint arXiv:2501.02576*, 2025.
- [46] J. Uhrig, N. Schneider, L. Schneider, U. Franke, T. Brox, and A. Geiger. Sparsity invariant cnns. In *2017 international conference on 3D Vision (3DV)*, pages 11–20. IEEE, 2017.
- [47] R. Upadhyay, H. Zhang, Y. Ba, E. Yang, B. Gella, S. Jiang, A. Wong, and A. Kadambi. Enhancing diffusion models with 3d perspective geometry constraints. In *ACM Transactions on Graphics (TOG)*, volume 42, pages 1–15. ACM New York, NY, USA, 2023.
- [48] M. Viola, K. Qu, N. Metzger, B. Ke, A. Becker, K. Schindler, and A. Obukhov. Marigold-dc: Zero-shot monocular depth completion with guided diffusion. In *arXiv preprint arXiv:2412.13389*, 2024.

- [49] D. Wofk, R. Ranftl, M. Müller, and V. Koltun. Monocular visual-inertial depth estimation. In *2023 IEEE International Conference on Robotics and Automation (ICRA)*, pages 6095–6101. IEEE, 2023.
- [50] A. Wong, S. Cicek, and S. Soatto. Targeted adversarial perturbations for monocular depth prediction. In *Advances in neural information processing systems*, volume 33, pages 8486–8497, 2020.
- [51] F. Yang, C. Feng, Z. Chen, H. Park, D. Wang, Y. Dou, Z. Zeng, X. Chen, R. Gangopadhyay, A. Owens, et al. Binding touch to everything: Learning unified multimodal tactile representations. In *Proceedings of the IEEE/CVF Conference on Computer Vision and Pattern Recognition*, pages 26340–26353, 2024.
- [52] G. Yang, H. Tang, M. Ding, N. Sebe, and E. Ricci. Transformer-based attention networks for continuous pixel-wise prediction. In *Proceedings of the IEEE/CVF International Conference on Computer vision*, pages 16269–16279, 2021.
- [53] L. Yang, B. Kang, Z. Huang, X. Xu, J. Feng, and H. Zhao. Depth anything: Unleashing the power of large-scale unlabeled data. In *Proceedings of the IEEE/CVF Conference on Computer Vision and Pattern Recognition*, pages 10371–10381, 2024.
- [54] L. Yang, B. Kang, Z. Huang, Z. Zhao, X. Xu, J. Feng, and H. Zhao. Depth anything v2. In *arXiv preprint arXiv:2406.09414*, 2024.
- [55] W. Yin, X. Wang, C. Shen, Y. Liu, Z. Tian, S. Xu, C. Sun, and D. Renyin. Diversedepth: Affine-invariant depth prediction using diverse data. In *arXiv preprint arXiv:2002.00569*, 2020.
- [56] W. Yin, C. Zhang, H. Chen, Z. Cai, G. Yu, K. Wang, X. Chen, and C. Shen. Metric3d: Towards zero-shot metric 3d prediction from a single image. In *Proceedings of the IEEE/CVF International Conference on Computer Vision*, pages 9043–9053, 2023.
- [57] C. You, Y. Mint, W. Dai, J. S. Sekhon, L. Staib, and J. S. Duncan. Calibrating multi-modal representations: A pursuit of group robustness without annotations. In *2024 IEEE/CVF Conference on Computer Vision and Pattern Recognition (CVPR)*, pages 26140–26150. IEEE, 2024.
- [58] Z. Zeng, D. Wang, F. Yang, H. Park, S. Soatto, D. Lao, and A. Wong. Worddepth: Variational language prior for monocular depth estimation. In *Proceedings of the IEEE/CVF Conference on Computer Vision and Pattern Recognition*, pages 9708–9719, 2024.
- [59] Z. Zeng, Y. Wu, H. Park, D. Wang, F. Yang, S. Soatto, D. Lao, B.-W. Hong, and A. Wong. Rsa: Resolving scale ambiguities in monocular depth estimators through language descriptions. In *arXiv preprint arXiv:2410.02924*, 2024.
- [60] C. Zhang, W. Yin, B. Wang, G. Yu, B. Fu, and C. Shen. Hierarchical normalization for robust monocular depth estimation. In *Advances in Neural Information Processing Systems*, volume 35, pages 14128–14139, 2022.
- [61] R. Zhang, Z. Zeng, Z. Guo, and Y. Li. Can language understand depth? In *Proceedings of the 30th ACM International Conference on Multimedia*, pages 6868–6874, 2022.
- [62] X. Zhang, B. Ke, H. Riemenschneider, N. Metzger, A. Obukhov, M. Gross, K. Schindler, and C. Schroers. Betterdepth: Plug-and-play diffusion refiner for zero-shot monocular depth estimation. In *arXiv preprint arXiv:2407.17952*, 2024.
- [63] W. Zhao, Y. Rao, Z. Liu, B. Liu, J. Zhou, and J. Lu. Unleashing text-to-image diffusion models for visual perception. In *Proceedings of the IEEE/CVF International Conference on Computer Vision*, pages 5729–5739, 2023.
- [64] R. Zhu, C. Wang, Z. Song, L. Liu, T. Zhang, and Y. Zhang. Scaledepth: Decomposing metric depth estimation into scale prediction and relative depth estimation. In *arXiv preprint arXiv:2407.08187*, 2024.
- [65] X. Zhu, R. Zhang, B. He, Z. Guo, Z. Zeng, Z. Qin, S. Zhang, and P. Gao. Pointclip v2: Prompting clip and gpt for powerful 3d open-world learning. In *Proceedings of the IEEE/CVF international conference on computer vision*, pages 2639–2650, 2023.

Supplementary Material

6 Evaluation Metrics

We evaluate our approach using the standard five error metrics and three accuracy metrics commonly adopted in prior works[42]. Specifically, the error metrics include absolute mean relative error (Abs Rel), square relative error (sq_rel), log error(\log_{10}), root mean squared error (RMSE), and its logarithmic variant (RMSE $_{\log}$). The accuracy metrics are based on the percentage of inlier pixels (δ) within three thresholds: $\delta_1 < 1.25$, $\delta_2 < 1.25^2$, and $\delta_3 < 1.25^3$.

- Abs Rel: $\frac{1}{M} \sum_{(i,j) \in \Omega} |\hat{d}_{pred}(i,j) - d_{gt}(i,j)| / d_{gt}(i,j)$
- sq_rel: $\frac{1}{M} \sum_{(i,j) \in \Omega} [(\hat{d}_{pred}(i,j) - d_{gt}(i,j)) / d_{gt}(i,j)]^2$
- RMSE: $\sqrt{\frac{1}{M} \sum_{(i,j) \in \Omega} (\hat{d}_{pred}(i,j) - d_{gt}(i,j))^2}$
- RMSE $_{\log}$: $\sqrt{\frac{1}{M} \sum_{(i,j) \in \Omega} (\log \hat{d}_{pred}(i,j) - \log d_{gt}(i,j))^2}$
- log $_{10}$: $\frac{1}{M} \sum_{(i,j) \in \Omega} |\log_{10}(\hat{d}_{pred}(i,j)) - \log_{10}(d_{gt}(i,j))|$
- D < thr: $(\max(\frac{\hat{d}_{pred}}{d_{gt}}, \frac{d_{gt}}{\hat{d}_{pred}}))$, thr = 1.25, 1.25 2 , 1.25 3

7 Quantitative Results on Sensitivity to Linguistic Description Variations

As shown in Tables 3 and 4, We quantitatively evaluated the inference results and sensitivity of the VGLD model to variations in linguistic descriptions. For both indoor and outdoor datasets, three images were used, with each image paired with three distinct textual descriptions. The corresponding visualization figures are provided in Figure 5 and 6. And the specific textual descriptions are provided in Tables 5 and 6.

From the tables, it is evident that the VGLD model demonstrates greater robustness when processing three different textual descriptions, while the RSA model exhibits larger errors. Moreover, under identical textual descriptions, VGLD consistently outperforms RSA.

Idx	Text-idx	Method	Abs Rel ↓	RMSE ↓	D1 ↑	pred_shift	LM_shift	pred_scale	LM_scale
1	Text-1	RSA[59]	0.210	0.689	0.263	1.255	1.193	1.032	1.026
		VGLD	0.080	0.240	0.987	1.207		1.020	
	Text-2	RSA[59]	0.110	0.367	0.995	1.220		1.028	
		VGLD	0.065	0.271	0.999	1.220		1.284	
	Text-3	RSA[59]	0.054	0.216	0.997	1.210		1.026	
		VGLD	0.052	0.232	0.997	1.216		1.025	
2	Text-1	RSA[59]	0.089	0.344	0.961	1.202	1.210	1.032	1.033
		VGLD	0.073	0.271	0.962	1.185		1.034	
	Text-2	RSA[59]	0.069	0.256	0.956	1.214		1.030	
		VGLD	0.063	0.272	0.962	1.213		1.037	
	Text-3	RSA[59]	0.064	0.296	0.947	1.218		1.036	
		VGLD	0.062	0.280	0.954	1.228		1.034	
3	Text-1	RSA[59]	0.251	0.868	0.138	1.331	1.218	1.042	1.034
		VGLD	0.147	0.433	0.920	1.254		1.041	
	Text-2	RSA[59]	0.055	0.240	0.993	1.199		1.035	
		VGLD	0.054	0.170	0.994	1.205		1.038	
	Text-3	RSA[59]	0.058	0.154	0.994	1.212		1.039	
		VGLD	0.055	0.138	0.994	1.199		1.035	

Table 3: Quantitative results on the NYUv2 dataset comparing VGLD and RSA in response to different textual descriptions. The yellow regions represent scalars values fitted using the Levenberg-Marquardt method. Best results are in **bold**.

Idx	Text-idx	Method	Abs Rel ↓	RMSE ↓	D1 ↑	pred_shift	LM_shift	pred_scale	LM_scale
1	Text-1	RSA[59]	0.097	4.060	0.926	1.005	1.003	1.011	1.010
		VGLD	0.075	3.562	0.949	1.004		1.001	
	Text-2	RSA[59]	0.084	4.251	0.923	1.007		1.010	
		VGLD	0.077	3.067	0.949	1.004		1.010	
	Text-3	RSA[59]	0.072	3.140	0.952	1.004		1.010	
		VGLD	0.068	3.088	0.951	1.004		1.010	
2	Text-1	RSA[59]	0.108	2.327	0.905	1.009	1.009	1.014	1.017
		VGLD	0.063	1.887	0.984	1.135		1.015	
	Text-2	RSA[59]	0.281	5.341	0.537	1.006		1.013	
		VGLD	0.099	2.144	0.915	1.010		1.014	
	Text-3	RSA[59]	0.109	2.157	0.906	1.011		1.014	
		VGLD	0.073	1.861	0.952	1.011		1.015	
3	Text-1	RSA[59]	0.268	6.526	0.740	1.004	1.008	1.009	1.011
		VGLD	0.119	2.516	0.919	1.009		1.010	
	Text-2	RSA[59]	0.171	4.479	0.854	1.005		1.010	
		VGLD	0.077	2.287	0.942	1.008		1.010	
	Text-3	RSA[59]	0.081	2.421	0.938	1.007		1.010	
		VGLD	0.062	2.236	0.953	1.009		1.011	

Table 4: Quantitative results on the KITTI dataset comparing VGLD and RSA in response to different textual descriptions. The yellow regions represent scalars values fitted using the Levenberg-Marquardt method. Best results are in **bold**.

Idx	Texts-idx	Text Description
1	Text-1	A man is standing in a doorway, looking at a bed with a striped comforter.
	Text-2	The bed is positioned in the corner of the room, with a man standing in the doorway, and a fish tank nearby.
	Text-3	A man stands in a doorway, looking into a bedroom with a large bed, a wooden dresser, and a fish tank.
2	Text-1	The image shows a classroom with a play area, a table with chairs, and a sink.
	Text-2	The image shows a classroom with a table, chairs, and a sink, all situated near a wall with bulletin boards and a window.
	Text-3	The image shows a classroom with a table, chairs, a sink, a bulletin board, a bookshelf, a window, and a rug.
3	Text-1	The image shows a red couch with towels hanging over the back, a flat screen television, and a framed jersey on the wall.
	Text-2	The image shows a red couch with a pink towel and a blue towel on it, positioned in front of a television with a framed jersey on the wall behind it.
	Text-3	The image shows a living room with a red couch, a flat screen TV, a framed jersey, and a guitar.

Table 5: The table shows three distinct textual descriptions provided for each image in the NYUv2 dataset, used as linguistic inputs for evaluating model sensitivity.

Idx	Text-idx	Text Description
1	Text-1	The image shows a narrow city street lined with parked cars and buildings on both sides.
	Text-2	The image shows a narrow street lined with parked cars and buildings, with a clear sky overhead.
	Text-3	The image shows a narrow street with parked cars on both sides, leading towards a building with a red awning.
2	Text-1	The image shows a narrow alleyway with a white gate at the end, a bridge overhead, and a hillside on one side.
	Text-2	The image shows a narrow alleyway with a white gate, a fence, a building, a bridge, and a sign, all situated in close proximity to each other.
	Text-3	A narrow alleyway with a white gate, a fence, a building, a bridge, a tree, a sign, and a hill.
3	Text-1	The image captures a lively street scene with people walking and riding bicycles, shops and buildings lining the street, and a clear blue sky overhead.
	Text-2	The image shows a narrow street in a European city, with buildings on both sides, a pedestrian walkway in the middle, and people walking and biking on the street.
	Text-3	The image shows a bustling city street with people walking and riding bicycles, shops and buildings lining the street, and a clear blue sky overhead.

Table 6: The table shows three distinct textual descriptions provided for each image in the KITTI dataset, used as linguistic inputs for evaluating model sensitivity.

8 Zero-shot Generalization

Benefiting from the smaller domain gap of language descriptions across diverse scenes[58, 59] and the ability of corresponding images to accurately indicate domain context, we conduct a zero-shot transfer experiment to demonstrate the generalization capability of VGLD. We evaluate the models on the SUN-RGBD[44], DIML Indoor[8], and DDAD[15] datasets without any fine-tuning. As shown in Figures 7, 8, 9 (qualitative results) and Tables 7, 8, 9 (quantitative results), VGLD consistently outperforms baseline methods and produces results that closely match those fitted by the LM method. This demonstrates that, under visual guidance, VGLD maintains stable scalars estimation and exhibits enhanced generalization capabilities. Note that all zero-shot experiments are conducted using the VGLD-NK-TCI model built upon the DAV1-vits RDE backbone.

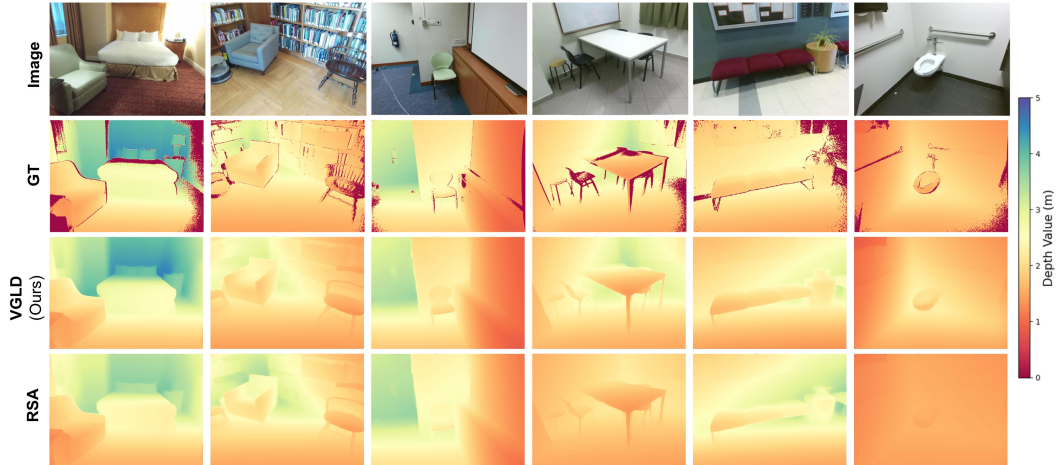


Figure 7: Zero-shot generalization on the SUN-RGBD dataset(Indoor). The models are evaluated without any fine-tuning. Benefiting from robust scale prediction, our VGLD method produces depth maps that are significantly closer to the ground truth compared to RSA.



Figure 8: Zero-shot generalization on the DIML Indoor dataset(Indoor). The models are evaluated without any fine-tuning. Benefiting from robust scale prediction, our VGLD method produces depth maps that are significantly closer to the ground truth compared to RSA.

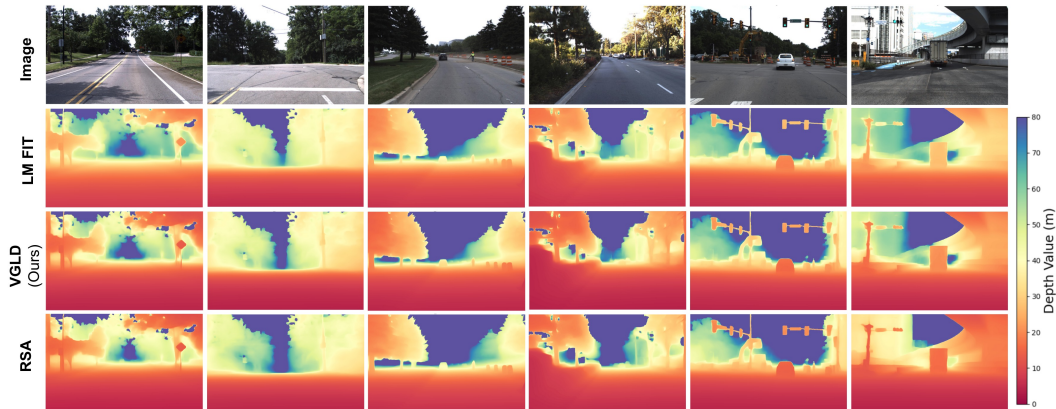


Figure 9: Zero-shot generalization on the DDAD dataset(Outdoor). The models are evaluated without any fine-tuning. Benefiting from robust scale prediction, our VGLD method produces depth maps that are significantly closer to the ground truth compared to RSA. Note that due to the sparse ground truth depth maps in the DDAD dataset, the visualization quality is poor. Therefore, LM Fit is used as a substitute for the ground truth depth map in the visualizations.

RDE Model	Method	Lower is better					Higher is better		
		Abs Rel ↓	sq_rel ↓	RMSE ↓	RMSE _{log} ↓	log ₁₀ ↓	D1 ↑	D2 ↑	D3 ↑
ZoeDepth[5]	robust depth estimation†	0.123	–	0.356	–	0.053	0.856	0.979	0.995
ScaleDepth[64]		0.129	–	0.359	–	–	0.866	–	–
	Least Squares	0.197	0.418	0.346	0.278	0.061	0.873	0.964	0.981
	Levenberg Marquardt	0.158	0.440	0.252	0.116	0.032	0.950	0.988	0.995
MiDas-1[6]	RSA-NK[59]	0.299	0.589	0.575	0.251	0.094	0.615	0.900	0.977
	VGLD-NK-T(Ours)	0.318	0.647	0.566	<u>0.242</u>	<u>0.089</u>	<u>0.643</u>	0.914	<u>0.980</u>
	VGLD-NK-I(Ours)	0.259	<u>0.595</u>	<u>0.468</u>	0.202	0.071	0.751	<u>0.957</u>	0.991
	VGLD-NK-TCI(Ours)	<u>0.262</u>	0.628	0.467	0.202	0.071	0.751	0.959	0.991
	Least Squares	0.203	0.419	0.365	0.272	0.062	0.860	0.961	0.981
	Levenberg Marquardt	0.173	0.438	0.291	0.132	0.039	0.926	0.984	0.994
MiDas-2[39]	VGLD-NK-T(Ours)	0.316	0.795	0.597	0.249	<u>0.090</u>	<u>0.639</u>	0.908	0.978
	VGLD-NK-I(Ours)	<u>0.288</u>	<u>0.688</u>	<u>0.552</u>	<u>0.246</u>	<u>0.090</u>	0.627	<u>0.922</u>	<u>0.984</u>
	VGLD-NK-TCI(Ours)	0.275	0.670	0.513	0.225	0.080	0.694	0.941	0.987
	Least Squares	0.194	0.418	0.337	0.305	0.062	0.880	0.963	0.980
	Levenberg Marquardt	0.146	0.439	0.224	0.103	0.027	0.961	0.989	0.995
DAV2-vits[54]	VGLD-NK-T(Ours)	0.304	0.742	0.564	<u>0.236</u>	<u>0.089</u>	<u>0.644</u>	0.920	<u>0.983</u>
	VGLD-NK-I(Ours)	<u>0.273</u>	<u>0.564</u>	<u>0.535</u>	<u>0.236</u>	0.090	0.617	<u>0.931</u>	<u>0.989</u>
	VGLD-NK-TCI(Ours)	0.241	0.545	0.433	0.189	0.067	0.779	0.967	0.993
	Least Squares	0.196	0.416	0.341	0.282	0.061	0.875	0.963	0.981
	Levenberg Marquardt	0.151	0.440	0.234	0.108	0.029	0.957	0.989	0.995
DAV1-vits[53]	RSA-NK[59]	0.290	<u>0.563</u>	0.571	0.250	0.092	0.640	0.899	0.969
	VGLD-NK-T(Ours)	0.281	0.583	0.532	0.214	0.078	0.711	0.945	0.987
	VGLD-NK-I(Ours)	<u>0.250</u>	0.573	<u>0.443</u>	<u>0.194</u>	<u>0.070</u>	<u>0.764</u>	<u>0.965</u>	<u>0.991</u>
	VGLD-NK-TCI(Ours)	0.241	0.545	0.433	0.189	0.067	0.779	0.967	0.993

Table 7: Zero-shot generalization to SUN-RGBD (Indoor). The yellow regions represent the results obtained using least-squares-type mathematical fitting methods. Best results are in **bold**, second best are underlined.

RDE Model	Method	Lower is better					Higher is better		
		Abs Rel ↓	sq_rel ↓	RMSE ↓	RMSE _{log} ↓	log ₁₀ ↓	D1 ↑	D2 ↑	D3 ↑
MiDas-1[6]	Least Squares	0.123	0.070	0.364	0.357	0.069	0.868	0.959	0.978
	Levenberg Marquardt	0.070	0.029	0.241	0.095	0.029	0.952	0.991	0.998
	RSA-NK[59]	0.219	<u>0.218</u>	0.667	0.246	0.096	0.612	0.882	0.964
	VGLD-NK-T (Ours)	0.251	0.385	0.683	0.240	0.094	0.622	0.898	0.969
	VGLD-NK-I (Ours)	0.188	<u>0.138</u>	0.544	0.208	0.079	0.696	0.943	0.982
	VGLD-NK-TCI (Ours)	<u>0.212</u>	0.281	<u>0.623</u>	<u>0.228</u>	<u>0.088</u>	<u>0.638</u>	<u>0.930</u>	<u>0.978</u>
MiDas-2[39]	Least Squares	0.133	0.080	0.394	0.345	0.071	0.846	0.954	0.977
	Levenberg Marquardt	0.086	0.039	0.285	0.114	0.036	0.929	0.988	0.996
	VGLD-NK-T (Ours)	0.243	<u>0.359</u>	0.737	<u>0.264</u>	0.100	0.585	0.877	0.964
	VGLD-NK-I (Ours)	<u>0.235</u>	<u>0.201</u>	<u>0.722</u>	0.294	<u>0.115</u>	0.460	<u>0.849</u>	<u>0.975</u>
DAV2-vits[54]	Least Squares	0.123	0.068	0.361	0.361	0.069	0.872	0.960	0.978
	Levenberg Marquardt	0.066	0.024	0.226	0.092	0.028	0.958	0.993	0.998
	VGLD-NK-T (Ours)	0.228	<u>0.300</u>	0.673	<u>0.246</u>	<u>0.096</u>	<u>0.593</u>	0.891	0.981
	VGLD-NK-I (Ours)	<u>0.212</u>	0.169	<u>0.663</u>	0.259	0.103	0.514	<u>0.899</u>	<u>0.989</u>
DAV1-vits[53]	VGLD-NK-TCI (Ours)	0.196	0.487	0.610	0.208	0.082	0.678	0.952	0.990
	Least Squares	0.118	0.063	0.345	0.344	0.066	0.875	0.961	0.979
	Levenberg Marquardt	0.056	0.020	0.203	0.081	0.024	0.970	0.994	0.999
	RSA-NK[59]	0.216	<u>0.283</u>	0.679	0.249	0.098	0.608	0.873	0.964
	VGLD-NK-T (Ours)	0.211	0.711	0.627	<u>0.215</u>	<u>0.084</u>	0.683	0.927	0.983
	VGLD-NK-I (Ours)	0.193	0.200	0.597	0.220	0.087	0.619	<u>0.950</u>	0.994
VGLD-NK-TCI (Ours)	<u>0.196</u>	0.487	<u>0.610</u>	0.208	0.082	<u>0.678</u>	0.952	<u>0.990</u>	

Table 8: Zero-shot generalization to DIML Indoor. The yellow regions represent the results obtained using least-squares-type mathematical fitting methods. Best results are in **bold**, second best are underlined.

RDE Model	Method	Lower is better					Higher is better		
		Abs Rel ↓	sq_rel ↓	RMSE ↓	RMSE _{log} ↓	log ₁₀ ↓	D1 ↑	D2 ↑	D3 ↑
MiDas-1[6]	Least Squares	0.123	0.070	0.364	0.357	0.069	0.868	0.959	0.978
	Levenberg Marquardt	0.070	0.029	0.241	0.095	0.029	0.952	0.991	0.998
	RSA-NK[59]	0.219	<u>0.218</u>	0.667	0.246	0.096	0.612	0.882	0.964
	VGLD-NK-T (Ours)	0.251	0.385	0.683	0.240	0.094	0.622	0.898	0.969
	VGLD-NK-I (Ours)	0.188	<u>0.138</u>	0.544	0.208	0.079	0.696	0.943	0.982
	VGLD-NK-TCI (Ours)	<u>0.212</u>	0.281	<u>0.623</u>	<u>0.228</u>	<u>0.088</u>	<u>0.638</u>	<u>0.930</u>	<u>0.978</u>
MiDas-2[39]	Least Squares	0.133	0.080	0.394	0.345	0.071	0.846	0.954	0.977
	Levenberg Marquardt	0.086	0.039	0.285	0.114	0.036	0.929	0.988	0.996
	VGLD-NK-T (Ours)	0.243	<u>0.359</u>	0.737	<u>0.264</u>	0.100	0.585	0.877	0.964
	VGLD-NK-I (Ours)	<u>0.235</u>	<u>0.201</u>	<u>0.722</u>	0.294	<u>0.115</u>	0.460	<u>0.849</u>	<u>0.975</u>
DAV2-vits[54]	Least Squares	0.123	0.068	0.361	0.361	0.069	0.872	0.960	0.978
	Levenberg Marquardt	0.066	0.024	0.226	0.092	0.028	0.958	0.993	0.998
	VGLD-NK-T (Ours)	0.228	<u>0.300</u>	0.673	<u>0.246</u>	<u>0.096</u>	<u>0.593</u>	0.891	0.981
	VGLD-NK-I (Ours)	<u>0.212</u>	0.169	<u>0.663</u>	0.259	0.103	0.514	<u>0.899</u>	<u>0.989</u>
DAV1-vits[53]	VGLD-NK-TCI (Ours)	0.196	0.487	0.610	0.208	0.082	0.678	0.952	0.990
	Least Squares	0.118	0.063	0.345	0.344	0.066	0.875	0.961	0.979
	Levenberg Marquardt	0.056	0.020	0.203	0.081	0.024	0.970	0.994	0.999
	RSA-NK[59]	0.216	<u>0.283</u>	0.679	0.249	0.098	0.608	0.873	0.964
	VGLD-NK-T (Ours)	0.211	0.711	0.627	<u>0.215</u>	<u>0.084</u>	0.683	0.927	0.983
	VGLD-NK-I (Ours)	0.193	0.200	0.597	0.220	0.087	0.619	<u>0.950</u>	0.994
VGLD-NK-TCI (Ours)	<u>0.196</u>	0.487	<u>0.610</u>	0.208	0.082	<u>0.678</u>	0.952	<u>0.990</u>	

Table 9: Zero-shot generalization to DDAD (Outdoor). The yellow regions represent the results obtained using least-squares-type mathematical fitting methods.

9 Ablation Study

9.1 Effect of the DRM

As shown in Table 10, we conduct ablation studies on the Domain Router Mechanism (DRM). The results demonstrate that the inclusion of DRM consistently improves the overall performance of VGLD and significantly enhances its cross-domain generalization capabilities.

RDE Model	Method	NYU			KITTI		
		Abs Rel↓	RMSE↓	D1↑	Abs Rel↓	RMSE↓	D1↑
MiDas-1[6]	w/o DRM	0.128	0.415	0.757	0.13	3.636	0.855
	with DRM	0.120	0.414	0.863	0.12	3.559	0.874
MiDas-2[39]	w/o DRM	0.158	0.513	0.740	0.19	4.987	0.728
	with DRM	0.151	0.513	0.780	0.18	4.804	0.737
DAV2-vits[54]	w/o DRM	0.135	0.459	0.798	0.163	4.060	0.767
	with DRM	0.127	0.434	0.835	0.153	3.980	0.772
DAV1-vits[53]	w/o DRM	0.122	0.437	0.847	0.145	4.327	0.748
	with DRM	0.112	0.392	0.883	0.136	4.008	0.816

Table 10: Performance comparison on NYU and KITTI datasets with and w/o DRM. Best results are in **bold**.

9.2 Effect of the LM loss

To investigate the effect of different weights of LM loss \mathcal{L}_{lm} on model training, we vary the value of α and train the VGLD-NK-TCI model based on the DAV1-vits RDE backbone. Evaluation on both the NYUv2 and KITTI datasets shown in Table 11 that the model achieves the best performance when $\alpha = 0.1$.

α	NYU			KITTI		
	Abs Rel↓	RMSE↓	D1↑	Abs Rel↓	RMSE↓	D1↑
0	0.115	0.403	0.874	0.164	4.856	0.781
0.001	0.116	0.413	0.869	0.161	4.204	0.779
0.01	<u>0.113</u>	0.399	<u>0.879</u>	<u>0.146</u>	<u>4.010</u>	<u>0.791</u>
0.1	0.112	0.392	0.883	0.136	4.008	0.816
1	0.115	<u>0.397</u>	0.868	0.162	4.701	0.778

Table 11: Ablation on LM loss for NYUv2 and KITTI datasets. Best results are in **bold**, second best are underlined.

9.3 Effect of the initial seeds.

To ensure the robustness of our training and verify that the results are not due to random initialization, we trained the model using three different random seeds. As illustrated in Figure 10, the resulting error bars indicate that variations due to different seeds are minimal, with nearly zero deviation.

10 Computational Complexity

As shown in Table 12, we present a comparison of model parameters and inference time between VGLD and RSA to quantify the computational resources required. All evaluations were conducted on a single NVIDIA RTX 3090 (24GB). The results indicate that the scalar predictor in VGLD is more lightweight than RSA. However, VGLD additionally incorporates a CLIP image encoder, which introduces an extra 14ms of inference time compared to RSA. Despite this overhead, VGLD offers a favorable trade-off: it achieves a 32.1% (Ref. to Tabel 1) improvement in Abs Rel on NYUv2 with an inference time of just 39ms and a modest parameter, making it a practical and efficient choice.

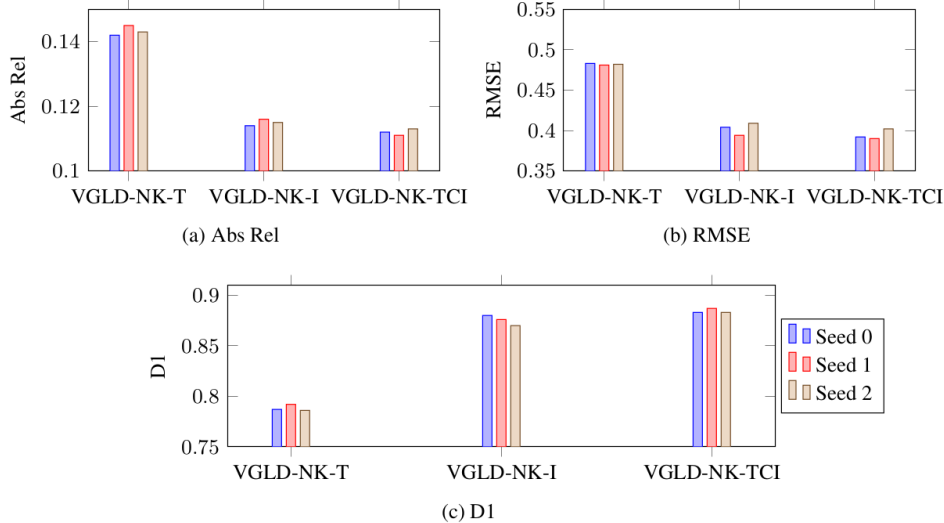


Figure 10: Error bars showing performance variations across different random seeds (0, 1, 2) for Abs Rel, RMSE, and D1 metrics. Each group of bars corresponds to a specific variant of the VGLD model.

Components	RSA[59]		VGLD (ours)	
	Params#	Inference Time	Params#	Inference Time
DAV1-vits[53]	24.78M	9.62ms	24.78M	9.62ms
CLIP Text Encoder[38]	63.43M	13.61ms	63.43M	13.61ms
CLIP Image Encoder[38]	-	-	86.19M	14.90ms
Scalars Predictor	1.49M	1.76ms	1.18M	0.94ms
Total	89.7M	24.99ms	175.58M	39.07ms
Increase / M (ms)	-	-	85.88M ↑	14.08ms ↑

Table 12: Computational Complexity Analysis. As shown in the table, the increase in model parameters and inference time of VGLD compared to the RSA model primarily stems from the additional CLIP Image Encoder component.

11 Prompts for Natural Text Generation

To generate natural and semantically rich image descriptions—rather than relying on fixed prompt templates—we employ two vision-language models: LLaVA-v1.6-Vicuna-7B and LLaVA-v1.6-Mistral-7B[20]. To ensure diversity in the generated captions, each model is prompted using six distinct instruction templates. These prompt templates are listed in Table 13.

Idx	Prompts
1	Summarize the image in one sentence.
2	Summarize the image in one sentence, focusing mainly on the proximity relationships of the objects.
3	Describe the image in one sentence from near to far, focusing on the absolute positions of objects, with no more than 8 categories.
4	Describe the image in one sentence from near to far, focusing on the objects' relative positions, with no more than 8 categories.
5	Summarize the image in one sentence, describing the overall spatial layout of the image.
6	Summarize the image in one sentence, describing the overall distance relationships in the image.

Table 13: Prompts for Natural Text Generation. We utilize two LLaVA models, each generating 6 textual descriptions per image, resulting in a total of 12 diverse descriptions for each image.